UNIVERSITY OF LEEDS

This is a repository copy of *Impact of Structural Binding Energies on Dissolution Rates for Single Faceted-Crystals*.

White Rose Research Online URL for this paper:
https://eprints.whiterose.ac.uk/177558/

Version: Accepted Version

Article:
Najib, M, Hammond, RB, Mahmud, T orcid.org/0000-0002-6502-907X et al. (1 more author) (2021) Impact of Structural Binding Energies on Dissolution Rates for Single Faceted-Crystals. Crystal Growth & Design, 21 (3). pp. 1482-1495. ISSN 1528-7483

https://doi.org/10.1021/acs.cgd.0c01142

© 2021 American Chemical Society. This document is the Accepted Manuscript version of a Published Work that appeared in final form in Crystal Growth & Design, copyright © American Chemical Society after peer review and technical editing by the publisher. To access the final edited and published work see https://doi.org/10.1021/acs.cgd.0c01142. Uploaded in accordance with the publisher's self-archiving policy.

Reuse
Items deposited in White Rose Research Online are protected by copyright, with all rights reserved unless indicated otherwise. They may be downloaded and/or printed for private study, or other acts as permitted by national copyright laws. The publisher or other rights holders may allow further reproduction and re-use of the full text version. This is indicated by the licence information on the White Rose Research Online record for the item.

Takedown
If you consider content in White Rose Research Online to be in breach of UK law, please notify us by emailing eprints@whiterose.ac.uk including the URL of the record and the reason for the withdrawal request.

White Rose university consortium
Universities of Leeds, Sheffield & York

eprints@whiterose.ac.uk
https://eprints.whiterose.ac.uk/

Impact of Structural Binding Energies on Dissolution Rates for Single Faceted-Crystals

Muhammad Najib [a]*, *Robert B. Hammond* [a], *Tariq Mahmud* [a], *Toshiko Izumi* [b]

[a]Center for Doctoral Training in Complex Particulate Products and Processes (CDT CP3), School of Chemical and Process Engineering, The University of Leeds, Leeds LS2 9JT, UK

[b]Pfizer Research & Development UK, Ramsgate Road, Sandwich, Kent, CT13 9NJ, UK

ABSTRACT

This study investigates the effect of solid-state intermolecular binding energies on the dissolution rates of single faceted crystals. The non-steroidal anti-inflammatory drug (NSAID) ibuprofen is employed in 95% v/v ethanol: water solution as a model system for single-crystal dissolution experiments in a dissolution cell at undersaturation ranging from 1.36% to 8.67%. In vitro dissolution of the ibuprofen crystals is quantified by capturing images during the dissolution process at fixed time intervals using a camera mounted on an inverted optical microscope. The regression rate of crystal faces with time is measured by image analysis. VisualHabit (VH) software is used for prediction of crystal morphology and to characterize the intermolecular binding energies in the solid-state structure of the ibuprofen crystals to predict relative, face-specific dissolution rates. The relative face-specific dissolution rates of ibuprofen crystal calculated based on binding energies suggest that the face (011) dissolves faster than face (002).

The experimental results on face-specific dissolution rates of single ibuprofen crystals reveal that the dissolution rates of faces (011) and (002) change non-linearly as a function of undersaturation. The binding energy model is critically evaluated for performance as confronted with the experimental measurements. The binding energy model suggests a pathway to understand dissolution at the microscopic level and to design a crystal morphology for regulating bioavailability optimally during dissolution processes.

1 INTRODUCTION

The overall market value of the pharmaceutical industry is expected to grow to $1.12 trillion by 2022[1]. Oral formulations make up more than 50% of pharmaceutical drugs when categorized based on the mode of administration [2]. Solid tablets are the most accepted form of oral formulations due to ease of ingestion and patient compliance [3]. When a fast disintegrating tablet is swallowed, it disintegrates into granules and then de-aggregates into primary particles of the active pharmaceutical ingredient (API). The primary API crystals are geometrical arrangements of molecules in three dimensions and are bounded by surfaces which have different chemical and physical properties according to their orientation as described by miller indices (*hkl*). The bioavailability of the API in the human body is ultimately dependent on the dissolution rate of API crystals and the rate of permeation of the API molecules through lipid membranes [4].

Dissolution is a process by which atoms, ions, or molecules detach from the surface of a solute crystal and enter the surrounding solution medium [5,6]. The phenomenon of dissolution is controlled by the surface kinetics (detachment of molecules from the crystal faces), mass transport (diffusion through concentration boundary layer), or by a mixed-regime [7]. Dissolution in mixed-regime is controlled by both surface kinetics and diffusional transport of molecules from the crystal-solution

interface to the bulk of the solution. The APIs belonging to class II and IV of the biopharmaceutical classification system (BCS) show low aqueous thermodynamic solubility and surface kinetics plays a significant role in their dissolution rates [8]. As the number of drug candidates showing poor aqueous solubility has reached approximately 70% [9] of all new drug candidates, it has become increasingly important to better understand the dissolution phenomena.

The dissolution of the API crystal population is often carried out in the industry as a key drug testing and quality control procedure [10]. This involves bulk solution concentration measurement as a function of dissolution time. This approach is useful in calculating average dissolution rates of the population of API crystals [11,12], but the contribution from single crystals is not recognized. Single crystals have various unique faces and the dissolution rates of the crystals of the same API could be different. This variation may arise due to different morphologies of the crystals, as every crystal face has a different orientation of molecular functional groups [13–16]. Thus, an understanding of the relative propensity of a molecule to detach from a crystal surface is important for the understanding of the dissolution process. The relative propensity of detachment can be used to assess relative dissolution rates of different faces of a crystals [17]. While there is a lot of literature on in-silico [18–25] and experimental [26–29] relative growth rates of different faces of crystals, the data on the relative face-specific dissolution rates of API crystals are scarce. The growth predictions are often related to the morphology of the crystals based on various models including Bravais-Friedel-Donnay and Harker (BFDH)[30] and attachment energy[31] models.

Experimental measurements of the face-specific dissolution rates of the API single crystals are, typically, carried out in closed dissolution cells [32–34], or in an open petri dish [35–37]. The solution medium is mostly static during single crystal observations [34–37], though different hydrodynamic conditions have also been reported [32,33]. The techniques to measure the dissolution rates include

interferometers [35], UV imaging [34], atomic force microscopy (AFM) [37], scanning ion-conductance microscopy (SICM) [36], or optical microscopy [32,33,38]. Most of the techniques measure two-dimensional data and any crystal faces which are sitting parallel to the bottom of the dissolution cell, or are tilted at some angle to the objective lens, are difficult to measure.

Dissolution has been modelled by various researchers but most of these models are extensions of the Noyes-Whitney equation [39] here labelled equation 1.

$$\frac{dm}{dt} = \frac{DA}{\delta}(C_s - C_b) \quad (1)$$

Where D= diffusion coefficient; A=total surface area; C_s= saturation solubility; C_b= bulk concentration and δ= boundary layer thickness.

Dissolution models have been beneficial to understand and predict the dissolution phenomena for better product design and control, but they come with certain limitations. These models assume a single undifferentiated interface of the particles with the solution and therefore single saturation solubility is used to predict the dissolution rates. These models also assume constant surface area and surface condition, continuous stirring, thin stagnant concentration boundary layer, diffusion-controlled mass transport mechanism, dissolution rate proportional to a concentration driving force and do not incorporate structural or interfacial chemistry.

Computational approaches such as molecular dynamics have been used to study different aspects of the dissolution of crystals [18,35,36,38,40–42]. Atomistic models of the crystal surfaces are generated and then solvated with a solvent to predict dissolution rates. The effects of corners on dissolution rates have also been predicted in MD simulations recently [18]. The predictions of relative face-specific dissolution rates of API crystals are not available, generally, except for a recent paper on aspirin [18]. The wetting aspect of the dissolution has also been explored recently in a solid-state

computational approach [43]. The molecules inside the crystal lattice are arranged according to spacegroup symmetry and form intermolecular interactions or bonds. The physiochemical properties of the crystals can be attributed to the molecules and molecular arrangements inside the crystal lattice. Dissolution rates are therefore linked to the arrangement of the molecules inside the crystal lattice.

An understanding of the dissolution at the single crystal level is not adequate to fill the knowledge gap and there is a need for a better computational approach that takes account of the anisotropy of the surfaces. Herein a new approach is described to measure semi-quantitative relative, face-specific dissolution rates of single API crystals based on solid-state intermolecular binding energies. These predictions are made in a vacuum assuming equivalent wetting of the crystal faces. The relative dissolution-rate predictions made this way can be used in conjunction with overall experimental dissolution rates of single crystals to extract absolute, face-specific dissolution rates. The results of the predicted relative, face-specific dissolution rates are validated against experimental data which are collected for single ibuprofen crystals in static 95% v/v ethanol: water solution using a dissolution cell and inverted optical microscope.

2 PROPOSED BINDING ENERGY MODEL

2.1 Background

Hartman and Perdok correlated crystal structure and morphology using bond energies in the attachment energy model back in 1955[31,44]. The attachment energy model states that the growth rate of a crystal face with Miller index (*hkl*) is proportional to the attachment energy E_{att} released when a growth slice of energy E_{sl} and thickness d_{hkl} is attached to an existing growing face i.e.

$$R \propto E_{att} \qquad (2)$$

A slice is a slab of crystal bounded by two adjacent parallel reciprocal lattice planes (*hkl*) and the respective interplanar spacing is denoted by slice thickness d_{hkl}. E_{sl} is the sum of the interaction energies between atoms of a central reference molecule in a slice of thickness d_{hkl} with the atoms of the other molecules within the same slice. E_{att} is the sum of the interaction energies of the atoms of the central reference molecule with atoms of the other molecules outside the slice. The face with the smallest absolute attachment energy grows at the slowest rate and the face with the greatest absolute attachment energy grows at the fastest rate. The attachment energies are converted to relative growth rates by simply taking their ratios [45,46] as in Equation 3.

$$R_{rel,g} = \frac{R_{i,g}}{R_{j,g}} = \frac{E_{att_i}}{E_{att_j}} \quad (3)$$

Where i and j are the faces of a crystal and j is more stable and taken as a reference.

$R_{rel,g}$ = relative growth rate of face i with respect to face j; $R_{i,g}$ = growth rate of face i; $R_{j,g}$ = growth rate of face j; E_{atti} = attachment energy of face i, E_{attj} = attachment energy of face j.

Perpendicular lines are drawn from the center of the crystal to the expected faces with lengths proportional to the relative growth rates and a final morphology is obtained according to Wulff plot [47]. The attachment energies, relative growth rates, and relative face to crystal center distances are based on intermolecular interactions within the crystal structure. Ziva Berkovitch and Yellin [45] calculated the intermolecular interactions between a central reference molecule and the other molecules within the crystal and defined the sum of these interactions as crystal energy E_{cr}. The convergence limit for E_{cr} was determined by gradually increasing the size of the crystal until there was no significant decrease in the crystal energy with the further addition of the molecules. The intermolecular interactions were partitioned into slice energies (E_{sl}) and attachment energies (E_{att}) to predict relative growth rates of the crystal faces and the final morphology. The intermolecular

interaction energies which are used to predict relative growth rates of the faces can also be exploited to predict relative dissolution rates of the same faces if the dissolution process is assumed to be the reverse of growth. During the growth process, slices are attached in both positive and negative growth directions [48], or conversely, a crystal can be split into a succession of slices as proposed by Hartman and Bennema [46] and shown in Figure 1.

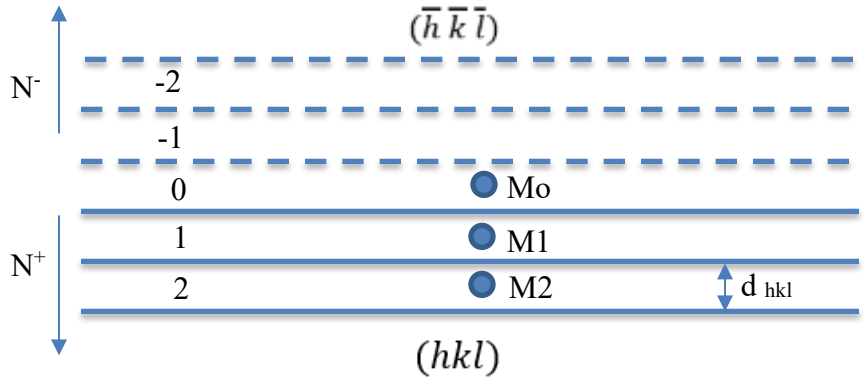

Figure 1 Shows 5 slices with slice 0 as the central slice and slices 1 and 2 in positive growth direction and slices -1 and -2 in the negative growth direction [45].

Where N^+= positive growth direction normal to planes (hkl); N^- = negative growth direction normal to planes $(\bar{h}\,\bar{k}\,\bar{l})$; d_{hkl}= interplanar spacing; M_o= molecule in central slice (slice 0); M_1= molecule in slice 1; M_2= molecule in slice 2.

The attachment energies in positive and negative growth directions of slice 0 are represented as $E_{att}(+)$ and $E_{att}(-)$ respectively according to the convention in the literature [49,50]. We maintain the positive growth direction as downwards in figure 1 following the original publication [46]. Faces (hkl) and $(\bar{h}\,\bar{k}\,\bar{l})$ are assumed chemically equivalent for example in centrosymmetric crystal systems and they express similar functional groups and molecular orientations, consequently, growth rate or dissolution rate of one face can be calculated to represent both. If the interactions

of the faces (hkl) and $(\bar{h}\,\bar{k}\,\bar{l})$ with the environment (impurities, solvent) or polarizability are neglected, then

$$E_{att}(+) = E_{att}(-) \quad (4)$$

The attachment energy model for crystal morphology prediction can be written as

$$E_{cr} = E_{sl}(hkl) + E_{att}(+) + E_{att}(-) \quad (5)$$

Where E_{cr} is a sum of the slice energy and the attachment energy in both positive and negative growth directions. If slice energy is greater, the attachment energy will be smaller and vice versa to keep the total crystal energy constant. Hartman and Bennema[46] used attachment energy approximation for larger d_{hkl} which states that

$$E_{att} \cong \sum iE_i \quad (6)$$

Where E_i is the interaction energy per molecule of a slice of thickness d_{hkl} with the i_{th} underlying slice. If i is taken as one, then according to figure 1, E_{01} represents interaction energy between slices 0 & 1. If i is 2, the interaction energy between slices 0 & 2 and -1 and 1 is E_{02} and E_{-11}. Bennema and Hartman ignored energies for $i \geq 2$ for larger values of d_{hkl}, as they were considered to have minimal impact on the final morphology. If only the positive growth direction is considered, then for i=1 to 2, the slice and attachment energies are related as:

$$E_{cr} > E_{sl}(hkl) + E_{att}(+) \quad (7)$$

Where E_{att} (+) $=E_{01} + E_{02}$. The attachment energy can also be defined as the fraction of total crystal energy released on the attachment of slices of thickness d_{hkl} to the growing surface [51]. In the context of this definition, the interaction energies E_{01} and E_{02} contribute a fraction of the total crystal energy. Since the intermolecular interaction energies in the crystal structure are a function

of the distance, therefore E_{01} contributes a greater percentage of the crystal energy than E_{02}, as the distance between slice 0 and 1 is $1*d_{hkl}$ and between slice 0 and 2 is $2*d_{hkl}$ i.e.

$$E_{01} > E_{02} \quad (8)$$

The slices in a crystal are arrangements of molecules in a 3D pattern. In figure 1, molecule M_o is located in the central slice 0, M_1 in slice 1, and M_2 in slice 2. The intermolecular interactions of the molecule M_o positioned in the central slice of the crystal with the other molecules in the crystal are saturated in a fully converged calculation and the addition of molecules to any face (hkl) of the crystal does not increase their crystal energy in a significant way. The molecule M_o is fully surrounded and tightly bound in its position and its interaction energy is approximately equal to the crystal energy ($E_{M0} \cong E_{crystal}$). To dislodge molecule M_o from the center of the crystal, an energy equivalent to crystal energy has to be expended. The molecule M_1 is located in slice 1 at a distance $1*d_{hkl}$ from the crystal center in the positive growth direction. The molecule M_1 is under-saturated and has fewer neighbors as compared to molecule M_o, consequently, M_1 is less strongly bound in the crystal lattice and therefore less energy is required to dislodge it from the crystal. Similarly, molecule M_2 is located in slice 2 at a distance $2*d_{hkl}$ from the central molecule M_o and is even less tightly bound to the crystal than molecule M_1. The binding interaction energy between molecules M_o and M_1 is greater than the binding interaction energy between molecules M_o and M_2 due to the greater distance between the pair mentioned later i.e.

$$E_{MoM1} > E_{MoM2} \quad (9)$$

Where E_{MoM1}= Interaction energy between molecules M_o and M_1.

Molecule M_2 is easier to dislodge from crystal structure than molecules M_1 and M_o respectively. The ease of removal is given in descending order as $M_2 > M_1 > M_0$.

From the above discussion, it is clear that the molecules/slices closer to the central molecule/slice contribute more to the crystal energy than the molecules/slices which are further away from the center of the crystal. The molecules in the slices closer to the central slice are more tightly bound and difficult to dislodge as compared to molecules in the slices away from the center. Since the molecules are not isotropic, so the strength of binding energy between the central reference molecule and surface molecules is different for different (hkl) faces.

2.2 Binding Energy Model

The proposed binding energy model is inspired by the attachment energy model but, instead, with the aim to predict relative, face-specific, dissolution rates of a crystal. When slices of thickness d_{hkl} are cut sequentially from different faces (hkl) of a crystal, the reference molecule in the central slice experiences a different rate of loss of binding energy for each face due to the anisotropic molecular interactions in the crystal as adjacent layers of molecules are removed. The loss in binding energy between the central reference molecule and the surface molecules is useful in predicting relative face-specific dissolution rates of the crystal. It is proposed that the relative dissolution rate perpendicular to a face (hkl) of the crystal is proportional to the binding energy loss when a slice of thickness d_{hkl} is removed from that face i.e.

$$\text{Relative dissolution rate of face (hkl)} \propto \text{Binding Energy Loss} \quad (10)$$

The ratios of binding energies of different faces represent their respective relative face-specific dissolution rates similar to attachment energy ratios representing relative face-specific growth rates.

The binding energies and distances between the central reference molecule and the other molecules in the positive growth direction are shown in Figure 2. The x-axis shows the distance from the central reference molecule to the other molecules in the positive growth direction in terms

of slice thicknesses d_{hkl}. The y-axis shows the cumulative binding energies between the central reference molecule and other molecules in the positive growth direction. The red curve with steps represents face 1 of the schematic crystal whereas the blue curve represents face 2. The molecules M1 to M5 are schematically arranged on the first step of the red curve in slice 1 and molecules M6 to M8 on step 2 of the curve are located in slice 2, whereas molecule M9 is located on step 3 and contributes to the crystal energy from slice 3. The horizontal length of each step along the x-axis

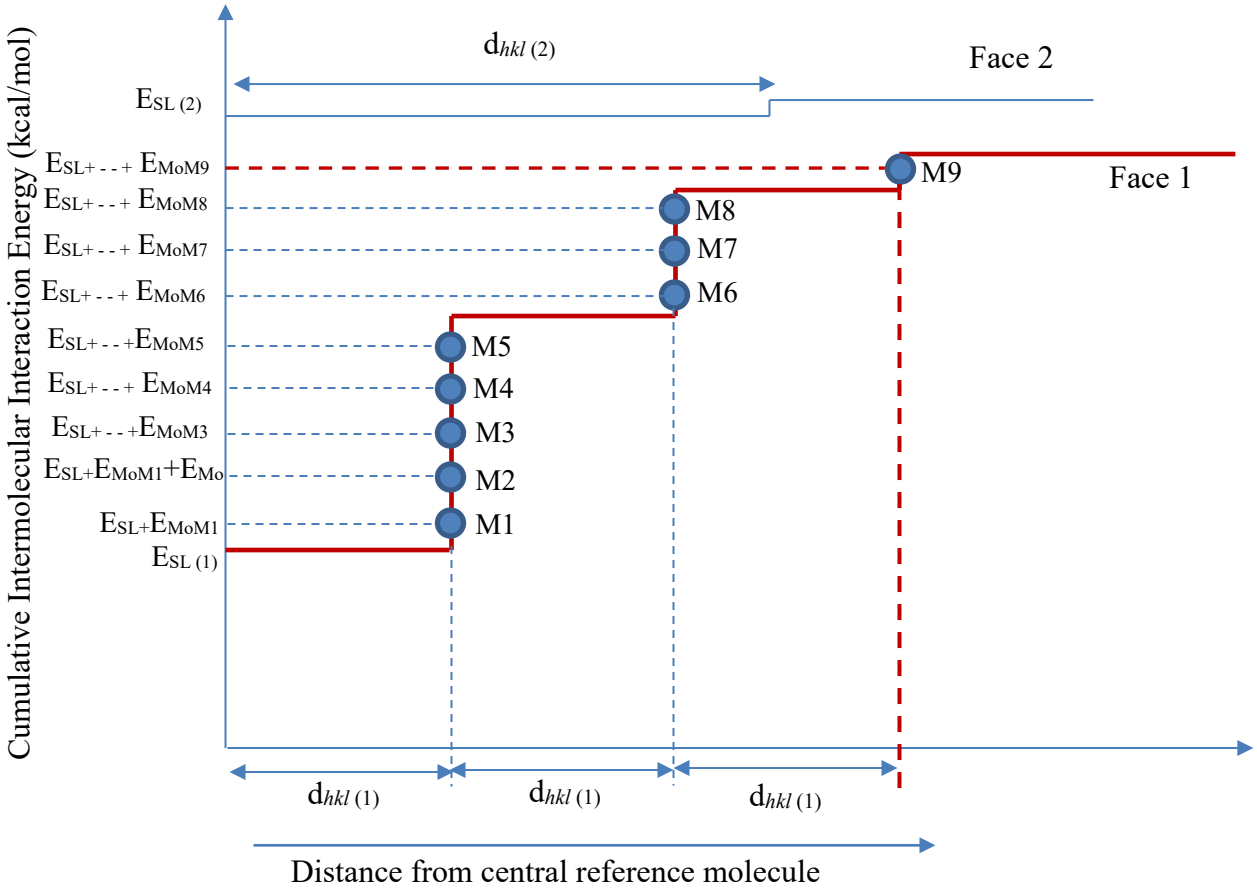

Figure 2 Arrangement of molecules in layers based on the distances from the reference molecule and the contributions of individual molecular binding energies in a schematic crystal.

represents a distance equal to one slice thickness (1*d_{hkl}). This is only valid if it is assumed that each slice creates only one energy step, but it may not be always true.

In some cases where the slice termination is (002) instead of (001) as in the ibuprofen crystal, or the asymmetric unit is not a single molecule, there might be two energy steps in one slice each with a horizontal distance on the figure equal to half of the slice thickness d_{hkl}. The vertical height of each step in the red curve shows the overall binding energy contribution from the molecules on that step. The individual energy contributions of molecules M1 to M5 on step 1 are shown. The schematic energy contributions by each molecule on the step are nearly equal in figure 2 whereas in a real crystal they will be different from each other i.e. some of the molecules M1 to M5 will contribute more energy than others due to slightly different distances from the reference molecule plane. The binding energy contributions of the molecules from M1 to M9 of face 1 start from $Esl+E_{MoM1}$ at a smaller value of cumulative energy on the y-axis and reach $Esl+E_{MoM1}+\ldots E_{MoM9}$, when the last contributing molecule for face 1 is added with the increasing summation radius. The limit for convergence has been chosen as -0.01 kcal/mol, the same as by Hartman [44]. Face 1 has a smaller E_{sl} value than face 2, but it has larger dynamic binding energy contributions from the subsequent slices added onto the central slice. For face 1, the dynamic range of the binding energy for all contributing molecules can be written as;

$$E_{B(hkl)} = \frac{E_{MoM1} + \cdots + E_{MoM9}}{3 * d_{hkl}} \qquad (11)$$

$$E_{B(hkl)} = \frac{\sum_{k=1}^{N} E_{MoMk}}{R_{MoMk}} \qquad (12)$$

Where E_{MoMk} = Interaction energy between reference molecule (M_o) in central slice and any other molecule (M_k). The value of k is from 1 to 9 in Figure 3 for face 1; R_{MoMk} = distance between

the central reference molecule and the kth molecule. In equation 12, $3*d_{hkl}$ has been replaced with R_{MoMk} to represent the cases with more than a single energy step in one slice.

It is obvious from equation (12) that every face (hkl) has different binding energy as the contributions of the molecules to the crystal energy in each (hkl) direction are different. The greater E_{sl} value for face 2 as compared to face 1, represents higher cohesion of the molecules in the slice and stronger intermolecular bonds. This can lead to greater hydrophobicity of the faces and it has been explained by molecular orientations in a recent study[43]. The face 2, therefore, has less dynamic energy contributions from any further slice additions. The dynamic binding energy contributions from slice additions on face 1 are greater as shown in figure 2 and therefore when a slice is removed from this face, there is a greater loss in the binding energy. The greater binding energy (E_b) values mean that there is a large part of the crystal energy which can be interpreted as the adhesive energy of the molecules in a given slice, with the molecules of the other slices. The molecules in higher binding/adhesive energy directions are more likely to switch bonds with the solvent molecules of similar nature when a crystal is dissolving. The (hkl) directions where binding energies are small have less adhesion as compared to the cohesion of the molecules inside the slices. A greater amount of energy is required to overcome the high cohesion of such molecules to make bonds with the solvent molecules to facilitate dissolution. The relative dissolution rates of the faces can be calculated as in equation 13.

$$R_{rel,D} = \frac{R_{i,D}}{R_{j,D}} = \frac{E_{b_i}}{E_{b_j}} \qquad (13)$$

Where $R_{rel,D}$ = Relative dissolution rate of face i to face j; $R_{i,D}$ = dissolution rate of the face I; and E_{bi} = binding energy of face i.

The effects of microscopic intermolecular binding energies are visible at the macroscopic level in the form of greater dissolution rates of some faces as compared to others.

The model treats the surface layer as a whole and does not capture the subcategories like kinks, edges, and steps. It is assumed that dissolution rates at the kinks and edges are much faster as compared to the layer removal mechanism and therefore are not rate-limiting.

3 MATERIALS AND METHODS

3.1 Materials

Racemic (R)-(S) ibuprofen (Figure 3a) with high purity (≥98%) was obtained from Tokyo Chemical Industry UK Ltd. A binary mixture of ethanol (Figure 3b) and water, obtained from Sigma Aldrich with azeotrope composition 95:5% by volume was used as a solvent. Ibuprofen was taken as a case study, as it produces a hexagonal plate-like morphology with well-defined faces for measuring face-specific dissolution rates. The azeotrope mixture was selected to minimize the effect of humidity during dissolution as the solvent mixture is expected to maintain

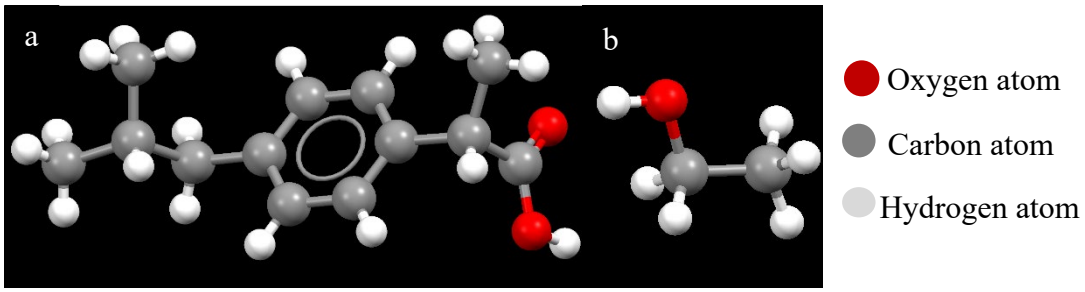

Figure 3 Molecular structures obtained from Mercury[55] for (a) ibuprofen; (b) ethanol

water content.

In addition to ibuprofen, a case study compound, furosemide, was selected from the literature[36] to test, further, the validity of the model proposed in this study. The selection of furosemide is in line with our focus on poor aqueous solubility APIs like ibuprofen. It has plate-like morphology with clearly identifiable faces and published face-specific dissolution rate data for single crystals under similar experimental conditions to those used in this study.

3.2 Gravimetric Solubility Measurement

Saturated solutions of (RS)-Ibuprofen in 95% v/v ethanol: water were prepared, with some excess solid content, in clear glass vials. The vials were agitated in a MaxQ 2000 Barnstead/Lab-line shaker for 20 hours. The temperature during the equilibration period was controlled through a Julabo F25 thermostat to an accuracy of ±0.1 °C. The solution was then allowed to settle for 6 hours. Two milliliters of the supernatant at 22 ℃, 29 ℃, 34 ℃, 39 ℃, and 44 ℃ was sampled and, on each occasion, transferred to a clean, glass petri dish using a preheated pipette at the same temperature as the solution. The solution samples were allowed to evaporate from the petri dish for two weeks until the mass of the solid content left in the petri dish no longer changed with time. The final mass in the petri dish was measured and the solubility was calculated.

3.3 Experimental set-up for Single Crystal Dissolution

The experimental setup [52] for the dissolution of single ibuprofen crystals is shown below in Figure 4. It includes a cell which houses a cuvette. The mechanical design of the cell is discussed in detail in literature [53]. The cuvette contains crystals of the ibuprofen in its saturated solution. The other parts of the equipment include a Leica water bath with a temperature control range of 10 to

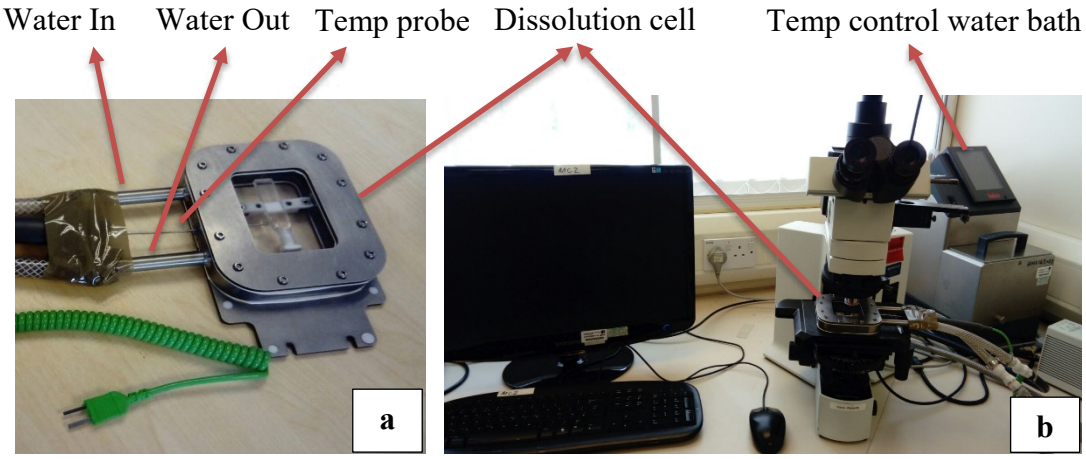

Figure 4 (a) Cell which houses the cuvette; (b) Experimental set-up for face specific dissolution rate measurement.

120 °C, an inverted polarising microscope, and a shallow water tank. The cell which houses the cuvette has two tubes attached to it for water entry and exit to maintain water temperature inside the cell. The temperature of the cell can be increased to create the desired degree of undersaturation to dissolve the crystals, whereas it can be reduced to create the desired degree of supersaturation to re-crystallize the ibuprofen. Images are captured with the camera mounted on the microscope at fixed time intervals until the face disappears. To measure the exact temperature of the solution inside the cuvette to establish the level of undersaturation, exact temperature measurement and control is required. This temperature is measured by inserting a thin wired, resistance temperature detector (RTD) into the dissolution cell. Figure 5 shows a schematic of the crystal lying inside the glass cuvette cell.

3.4 Experimental Procedure

A saturated solution of ibuprofen, with a solubility of 1.02 g/ml at 30 ℃, was prepared by adding the solute to 95% v/v ethanol: water mixture. Then one milliliter of this solution was measured with a pipette and transferred into the pre-heated cuvette. The cuvette was sealed with paraffin tape to stop any egress of the solution or ingress of contaminants. Then the cuvette was placed

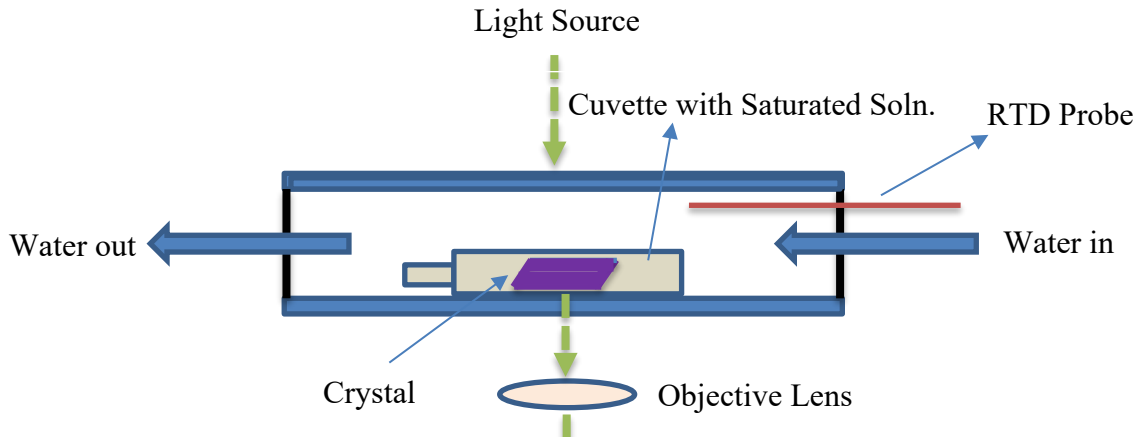

Figure 5 Schematic of the Cell with cuvette. The RTD probe enters into the cell through a wall entrance

inside the clear glass dissolution cell. The temperature of the dissolution cell was reduced to 25 ℃ to crystallize single crystals of ibuprofen. Once the required size of the crystals was achieved, the temperature of the cell was swiftly increased above 30 ℃ to create the desired degree of undersaturation for dissolution. The images were taken by a microscope camera at fixed intervals of time during dissolution until the crystal's edges started becoming rounded and lost their identity. A new stock-solution was used for the next experiment and this cycle continued until the desired amount of experimental data were collected. The dissolution experiments were repeated for different degrees of undersaturation. The rates of dissolution were measured by measuring the speed at which the faces receded by image analysis.

3.4.1 Image Analysis Methodology

The image analysis methodology to deduce face-specific dissolution kinetics is based on work published in literature 52,54. An indexed crystal of ibuprofen is shown in Figure 6. The crystal is lying flat on the face {100}. The side faces are {002} and the capping faces are {011}. Two

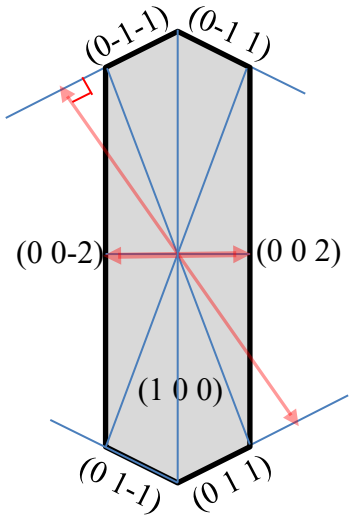

Figure 6 Schematic image of the crystal highlighting the methodology to measure face-specific dissolution rates

diagonal lines are drawn from the opposite capping faces {011} of the crystal along with lines along the maximum length and width of the crystal to mark the center point. The perpendicular distance from the center of the crystal to the face {002} is measured at each time interval to calculate the rate at which face {002} recedes overtime during the dissolution process. The normal distance from the center of the crystal to the projection of the face {011} is measured at a fixed time interval during dissolution to calculate the rate at which the face {011} dissolves.

3.5 Morphology and Binding Energy Calculation Methodology

3.5.1 Morphology Prediction

The crystal structure of the model molecule was accessed from the Cambridge Crystallographic Data Center (CCDC) using CCDC software Mercury[55]. The energy calculations were carried out in VisualHabit which is a plug-in application with Mercury and has been developed at the university of Leeds[56,57]. Lattice energy calculations for the APIs for each atomistic-potential scheme present in VisualHabit were compared against the sublimation enthalpy of the API to choose the most appropriate atomistic potential scheme which produced the closest match. The morphology of the API was then predicted based on the chosen potential scheme and the attachment energy model. The lattice energy convergence was checked to make sure that the selected radius for lattice interactions to converge was appropriate and that a stable lattice energy summation was generated.

3.5.2 Binding Energy Calculation Methodology

The molecular positions of the molecules and their interaction energies with other molecules inside the crystal structure were generated. A visualization of the intermolecular interaction energies is shown in Figure 7. For identifying the positions of the molecules, a dummy atom was

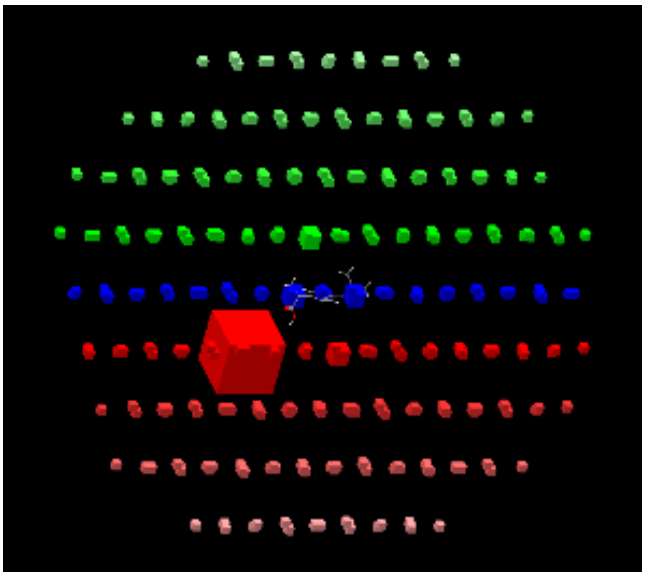

Figure 7 3D plot of the molecular positions. Red dot shows reference molecule

placed at the center of coordinates of each molecule in the positive growth direction for the binding energy calculations.

The shortest distances between the central plane, on which a reference molecule was located, to the molecules in the positive growth direction were calculated according to the method described in Figure S1 in supporting information. The energies of the molecules in the positive growth direction were added into the energy of the central growth slice in the same way as described in the binding energy calculation algorithm in Figure 8. The algorithm shows the steps suggested for binding energy calculations and the determination of relative dissolution rates of the crystal faces. The distances of the molecules from the reference plane were calculated and arranged in order of distance from the closest to the reference plane to the farthest away. The binding energy contributions of each molecule were then added as a function of the distance. The binding energy values of the crystal faces divided by their respective distances from the reference molecule to the last contributing molecule produced binding energy per unit length. The binding energy ratios of any two faces indicated their relative dissolution rate ratios.

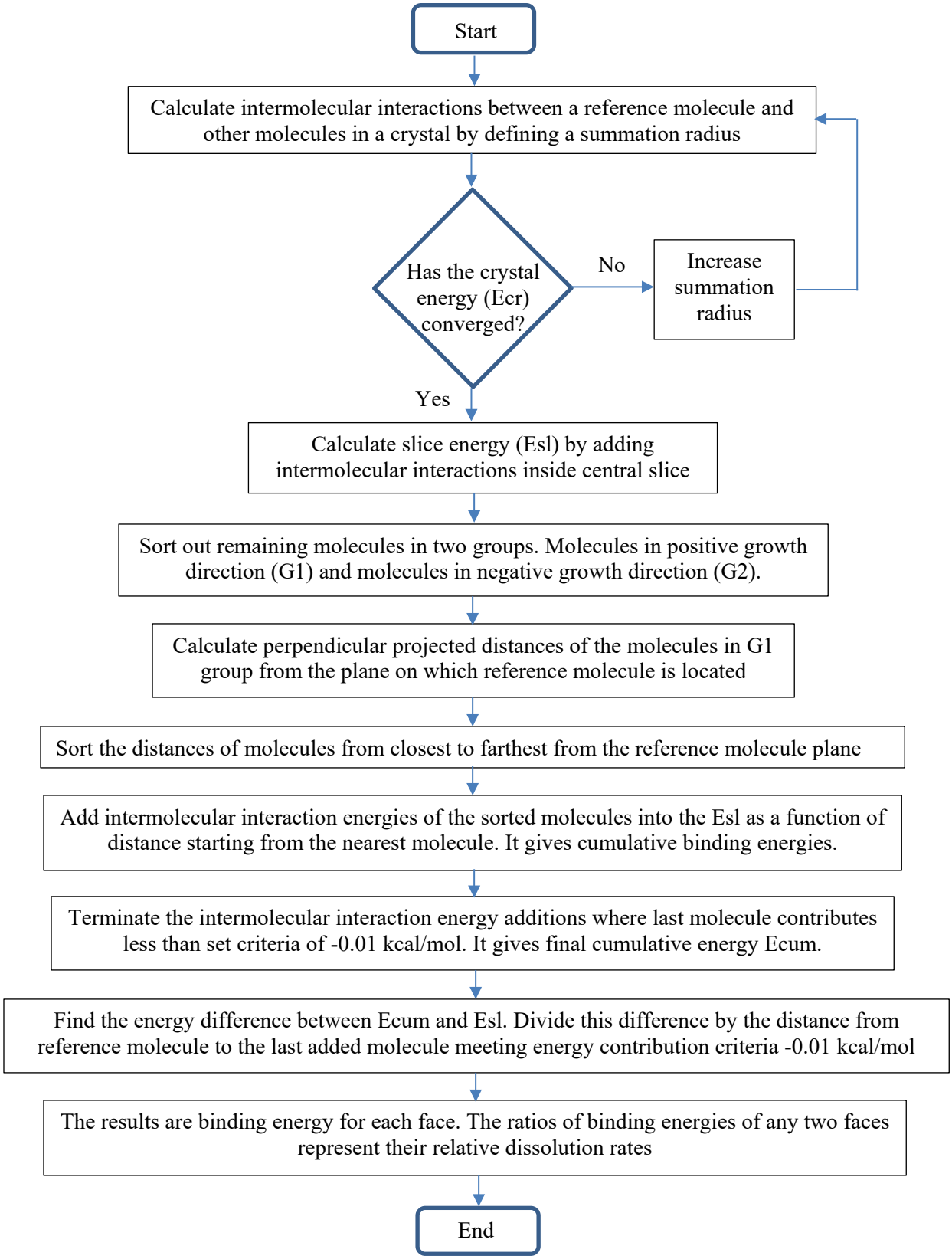

Figure 8 Algorithm showing calculation steps for the binding energy

In the case of ibuprofen, where the asymmetric unit was a single molecule, the above

methodology was carried out as described, but in the case of furosemide where the asymmetric unit was not a single molecule, a slightly different approach was used. In cases where there are two molecules in the asymmetric unit, the growth slice will have two layers of the molecules. In such situations, the central plane is taken as the one which sits closest to the crystal center and then energy contributions of other molecules are added one at a time as already described. This method was applied to the case of furosemide. Once the binding energy for each (hkl) direction of interest had been calculated, their ratios produced intrinsic relative face-specific dissolution rates of the crystal.

4 RESULTS AND DISCUSSION

4.1 Experimental Data Analysis

Ibuprofen was crystallized at 25 °C inside a fully sealed glass cuvette in a dissolution cell. Two polymorphic forms of racemic ibuprofen are reported in the literature [58]. Since a low driving force for crystallization was used in this work and the angles observed between faces are consistent with the unit cell parameters for form I, it is highly probable that polymorphic form I[58–61] was crystallized and present during the dissolution experiments. Ibuprofen shows a hexagonal morphology with the {100} face, sitting flat on the glass cuvette bottom. The capping faces are {011} and the side faces are {002}. Ibuprofen crystal indexing was carried out by comparing interfacial angles between predicted and experimental morphologies and single crystals, grown under similar conditions, have been indexed in literature[52]. An indexed crystal is shown in Figure 9. The experimentally observed morphology is consistent with the polymorphic form I. During the crystallization stage, when the crystal size was approximately 500 μm, the temperature was increased to undersaturate the solution to the desired degree of 1.36% to 8.67% to dissolve the crystals. Images were captured by a camera mounted on the inverted microscope at fixed time intervals during the process of dissolution of the ibuprofen crystals in 95% v/v ethanol: water

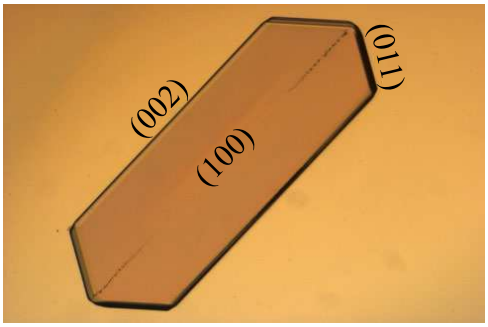

Figure 9 Indexed crystal of ibuprofen

solution as shown for an undersaturation of 5.09% in Figure 10. The data on the dissolution rates were recorded from the start of the dissolution process until the corners and edges of the crystals became rounded. It was observed that first corners and then edges of the crystals became rounded as can be seen in Figure 10. After 10 minutes of the dissolution process, the corners started disappearing and after 15 minutes the edges were very close to rounding off. In Figure 10, the dissolution data were collected for only the first 10 minutes of the dissolution for the face {011} and 15 minutes for the face {002}. A similar approach was used for all other data sets provided in the supporting information.

The face displacement accelerated with time during the dissolution process as seen from Figure 11. Higher index faces might have been exposed by the corner and edge rounding which increased the rate of the dissolution. Graphs showing the rate of recession of faces on ibuprofen single-

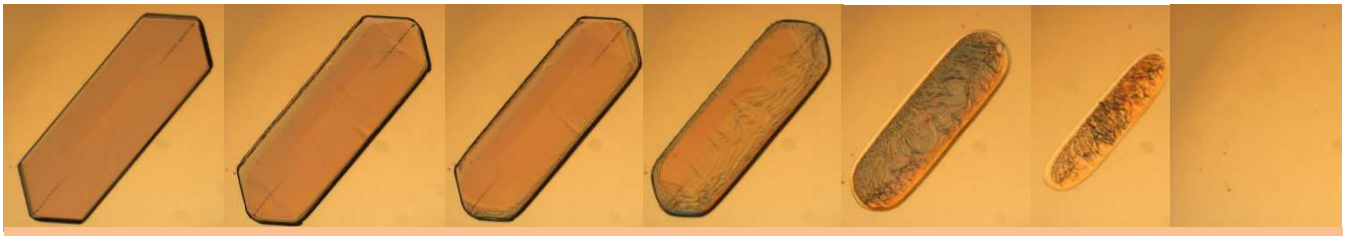

Figure 10 Images captured by the camera mounted on the microscope at fixed time intervals of 0, 5, 10, 15, 30, 45 and 53 minutes at undersaturation 5.09%.

crystals, included in the supplementary information, indicate that the degree of the nonlinearity of face displacement as a function of time was small for the duration of the measurement used to validate the predicted results. It is therefore expected that the effect of corner and edge rounding was minimal for the experimental results reported here.

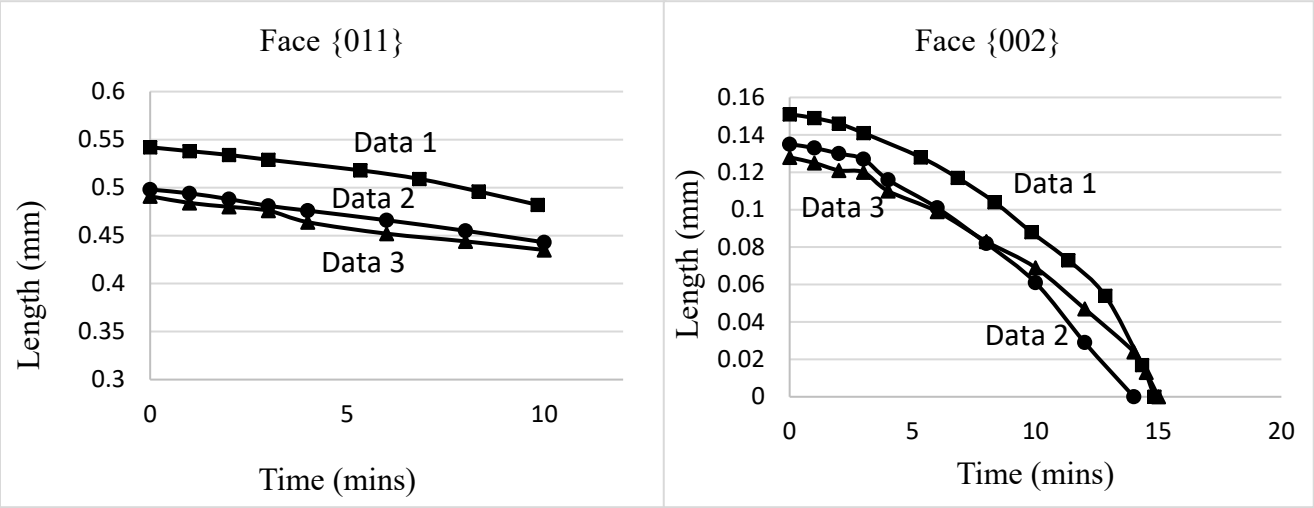

Figure 11 Rates of dissolution of faces {011} and {002} at undersaturation 5.09%. Dissolution rate of face {002} accelerates over time

The centre to face lengths were plotted against time and linear trends were fitted to find the dissolution rates (μm/min) of faces {011} and {002} for ibuprofen as shown in table 1. The dissolution rates (μm/min) were then plotted against % undersaturation as shown in Figure 12. It can be seen that the rate of dissolution (μm/min) varies non-linearly with the percentage undersaturation.

The dissolution rates (μm/min) of the faces {011} and {002} are smaller when the undersaturation is small (solution concentration is closer to saturation). As the degree of undersaturation is increased, the dissolution rates of both faces increase nonlinearly with a similar

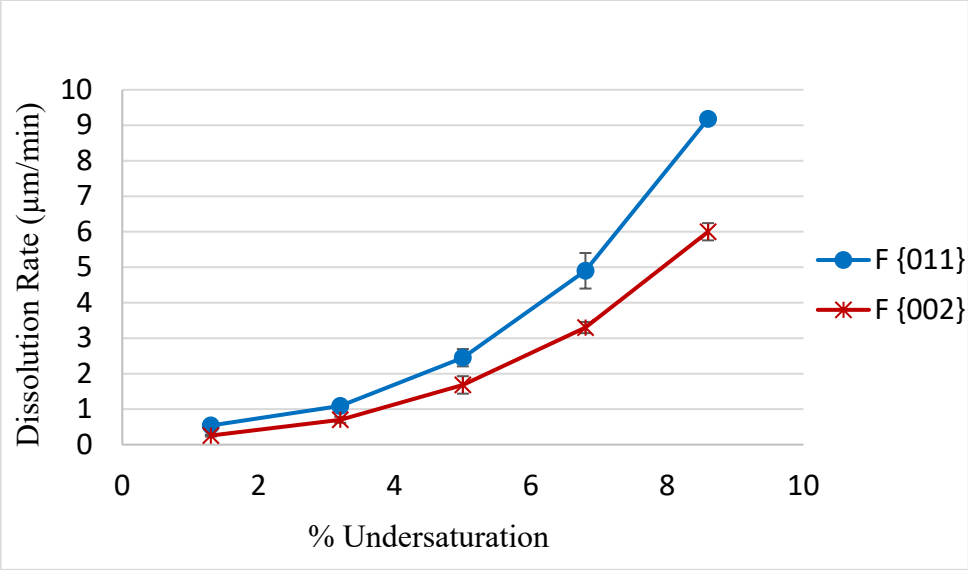

Figure 12 Rates of dissolution of faces {011} and {002} as a function of percentage undersaturation

Table 1 Rates of dissolution of faces {011} and {002} of ibuprofen in 95% ethanol as a function of undersaturation

Percentage Undersaturation, (σ %)	Face {011}		Face {002}		Ratio {011}/{002}
	Average (µm/s)	Std. Dev. (µm/s)	Average (µm/s)	Std. Dev. (µm/s)	
1.36	0.54	0.05	0.26	0.03	2.07
3.24	1.09	0.05	0.70	0.08	1.56
5.09	2.45	0.24	1.68	0.24	1.45
6.89	4.9	0.50	3.3	0.16	1.48
8.67	9.18	0.13	6.00	0.24	1.53

trend. The ratio of the dissolution rate (µm/min) of {011} to {002} varies from 2.07 at the smallest undersaturation to 1.53 at the greatest undersaturation. The average dissolution rate (µm/min) ratio of {011} to {002} faces over the whole undersaturation range remains nearly constant around 1.57

except for an undersaturation of 1.36%. The dissolution rates (μm/min) were converted to the face-specific flux (μmol/s.m^2) values and the results suggested that the smaller face {011} dissolved at a faster rate irrespective of the degree of the undersaturation as shown in the supporting information table S7.

4.2 Ibuprofen Morphology Prediction

The lattice energy of RS-ibuprofen (CCDC ref code: IBPRAC)[62] was calculated using various atomistic potential schemes including Momany, Gavezzotti, Dreiding II, and Tripos 5.2. The lattice energy was plotted as a function of the radial distance from a central molecule of the crystal as shown in Figure 13.

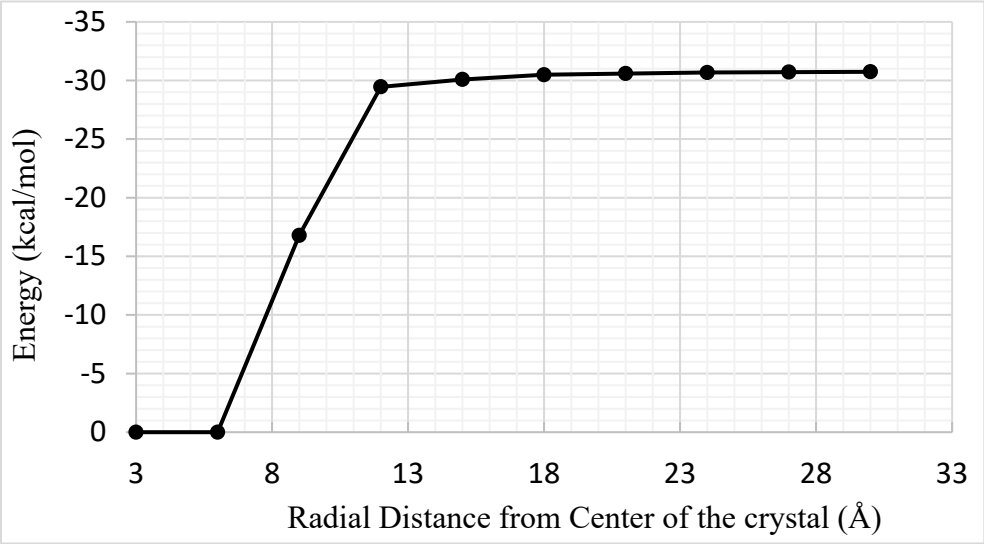

Figure 13 Lattice energy convergence calculated by attachment energy model using Dreiding II potential scheme.

The lattice energy converges at a distance of 18 Å from a central molecule of the crystal. The calculation was performed within a 30 Å radial cut-off distance, which means that a stable lattice energy determination was achieved. The atomistic potential scheme which gave the closest lattice energy match to the sublimation enthalpy was chosen and the morphology predicted based on that potential scheme. The calculated lattice energy using the Dreiding potential scheme was found to

be -30.73 kcal/mol which was in reasonable agreement with the enthalpy of sublimation -31.10 kcal/mol. The crystal forms of which the morphology is comprised are sets of faces that are rendered equivalent as a result of the spacegroup symmetry and have a similar orientation of molecules. The significant faces and subsets in the predicted morphology of RS-ibuprofen are {100} = {(100), (-100)}, {002} = {(002), (-002)} and {011} = {(011), (01-1), (0-11), (0-1-1)}. The morphology as can be seen from Figure 14, is plate-like as viewed from the top with the face (100) facing out of the page. The face with the largest area according to the prediction is (100). The faces (011) and (002) are also visible but have much smaller areas as compared to the face (100). The main faces (100), (011), and (002) have similar area ratios to each other as found in the experimental data, but the number of the faces shown in the predicted morphology is more than the experimental morphology. The experimental morphology is more elongated as compared to the predicted morphology. This difference is expected due to the effect of the crystal-growth environment. In VisualHabit the morphology is predicted in a vacuum and equivalent wetting is

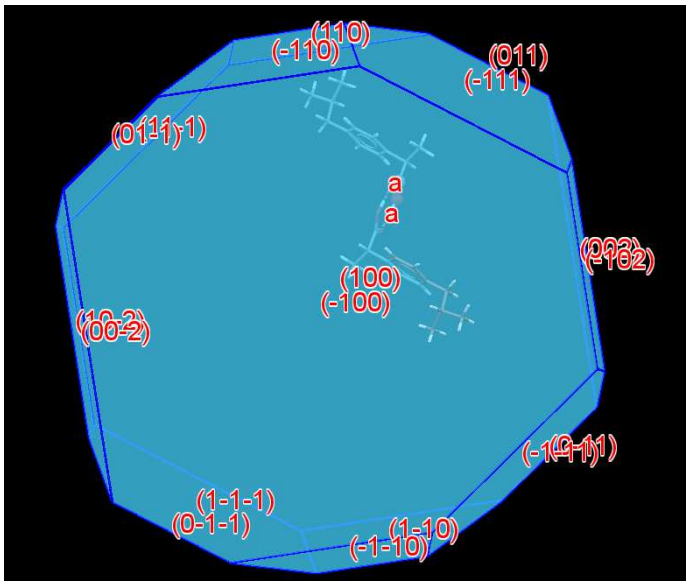

Figure 14 Ibuprofen morphology predicted by attachment energy model using Dreiding II potential scheme.

assumed, whereas, in experimental work, the environment is a saturated solution of ibuprofen in 95% ethanol: water. The relative wetting of the crystal face (011) is greater in the ethanol solvent as compared to the face (002). Since the solute molecules in the solution show stronger hydrogen-bond interactions with the face (011) as compared to the face (002), the growth in the direction of the face (011) is more than for the face (002) and the resulting morphology is more elongated when observed in experiments [43].

4.3 Binding Energy Analysis

Since VisualHabit uses atomistic potential fields, it calculates all of the intermolecular interaction energies during the lattice energy calculation. Figure 15 shows a 2D snapshot of the 3D coordination sphere with different molecules inside the predicted crystal structure of ibuprofen. The molecules are arranged in a layered pattern as expected. The layer with the blue colored

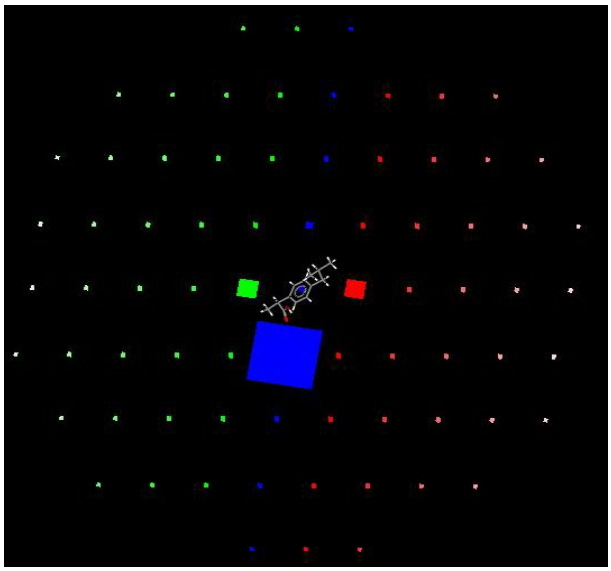

Figure 15 Molecules arranged in layers inside the crystal structure for face {002}, where blue color means molecules inside the central slice, red color means molecular slices in the positive direction whereas green color means slices in the negative direction. The size of the cubes represents the strength of interaction energy.

molecules shows that these molecules belong to the central slice, the molecules in the red colored slices are in the positive growth direction whereas the green-colored molecules are in the negative growth direction. The volumes of the cubes are proportional to the strength of the molecule-molecule interaction energy. The different sizes of the cubes indicate the intermolecular interaction anisotropy within the crystal lattice. For example, a big blue cube is present in Figure 15, which shows the strongest intermolecular interaction energy which is shown in the first row in table S1 in supporting information with a value of -7.491 kcal/mol. The other molecules show considerably smaller interaction energies as compared to this single strong interaction.

This strong interaction energy is due to the hydrogen bond (OH----O) between the central molecule and another molecule adjacent to it in the same slice as shown in table S1 in supporting information. The cumulative interaction energies were plotted as a function of distance starting from slice energy of the central slice and then adding intermolecular interaction energy of one molecule at a time as a function of the distance from center to the face as shown in Figure 16.

It can be noted that the slice energy of the face (011) is greater (ignoring negative sign) than the slice energy of the face (002). The curve of cumulative binding energies of the face (011) has a greater overall value than the face (002). The net binding energy, i.e. final cumulative binding energy minus the slice energy for the face (011) is -13.29 kcal/mol whereas for the face (002) it is -8.43 kcal/mol. The greater binding energy in the case of the (011) face is due to stronger hydrogen bond interactions for this face as compared to weaker dispersion forces in the direction of the face (002). The distance of the last molecule contributing -0.01 kcal/mol from central reference molecule to face (011) is 13.16 Å, whereas this distance is 10.87 Å for the face (002), as shown in table 2.

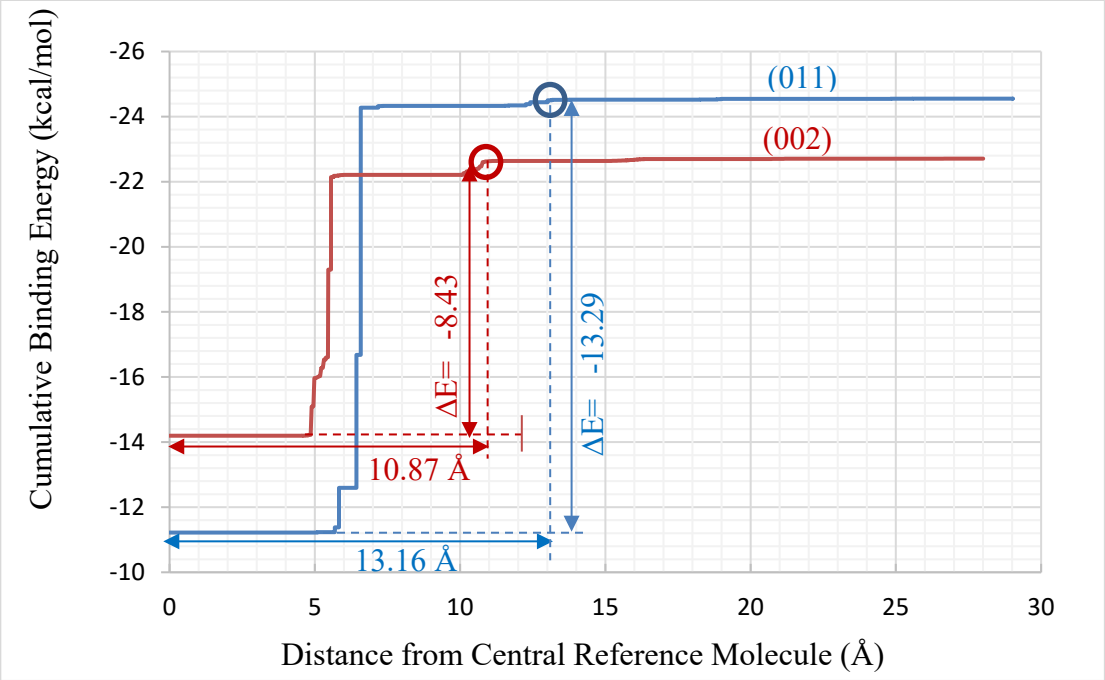

Figure 16 Binding energy loss as a function of distance from the center of the crystal to the face (hkl).

The binding energy per unit length for the face (011) is 1.009 kcal/mol.Å whereas for the face (002) it is 0.775 kcal/mol.Å. The greater binding energy per unit length is indicative of the faster dissolution rate. Since the face (011) has the greater binding energy per unit length as compared to face (002), it means that when a slice of molecules is removed from (011) face, the central reference molecule in the center of the crystal experiences a greater loss in the binding energy, therefore it is predicted to have the fastest dissolution rate.

Table 2 Binding Energy per Unit Length Calculations

Face (hkl)	Cumulative Binding Energy (kcal/mol)	Distance from Ref. Molecule to Surface (Å)	Binding Energy per Unit Length (kcal/mol.Å)
(011)	-13.29	13.16	1.009
(002)	-8.43	10.87	0.775

4.4 Validation of Experimental Results

The predicted and experimental dissolution-rate ratios of the face (011) to the face (002) are given in table 3. The predicted relative dissolution rate of the face (011) to the face (002) is 1.30, whereas the experimental value for this ratio is 1.50. The percentage deviation between predicted and experimental results is 13.3 %. The prediction by binding energy model is made in the vacuum, where, in the absence of any solvent, the equivalent wetting condition is applicable. In real experimental conditions, the environment for ibuprofen crystal dissolution was not a vacuum but instead an ethanol: water solution. The wetting of the faces (011) and (002) is different which leads to the discrepancy between experimental and predicted relative dissolution rates. The effect of corners and edges has also not been considered in the binding energy model, whereas it plays a role during the experimental dissolution.

Table 3 Validation of the Predicted Relative Dissolution Rates

	Dissolution Rate Ratio (011)/(002)	**% Deviation between Model and Experiment [(Exp.-Model)*100/Exp.]**
Binding Energy Model	1.30	-13.3
Experiment	1.50	

New, higher-index facets with small surface area and a small coordination number may appear during dissolution and accelerate the dissolution rate towards nonlinearity as has been suggested in the literature[36,37,63]. The binding energy model in its current, simple, form has not been applied to capture the new facets in an evolving morphology, instead, experimental conditions such as employing a small dissolution driving-force and a short time period during which dissolution images were captured have been used. Accordingly, the experimental, face-specific dissolution

rates are not affected significantly by any new faces which develop during dissolution. The small driving force during dissolution experiments is useful in enforcing a layer by layer dissolution mechanism as the rate-limiting process as compared to the faster dissolution rates on kink and edge sites which are not captured by the binding energy model. This enables the experiments to produce such dissolution rates, which can be used to validate the binding energy model predictions without going into details of the topology of the crystal surfaces.

5 CASE STUDY: FUROSEMIDE

The binding energy model was applied to the case study API molecule Furosemide (CCDC ref code: FURSEM03)[64], as published experimental data on the face-specific dissolution rates is available for this compound. The case study involves polymorphic form I of Furosemide which belongs to triclinic space group $P\bar{1}$ and BCS class IV. Figures 17 (a) and (b) are the experimental morphologies whereas the (c) and (d) are the predicted morphologies as given in the literature[36].

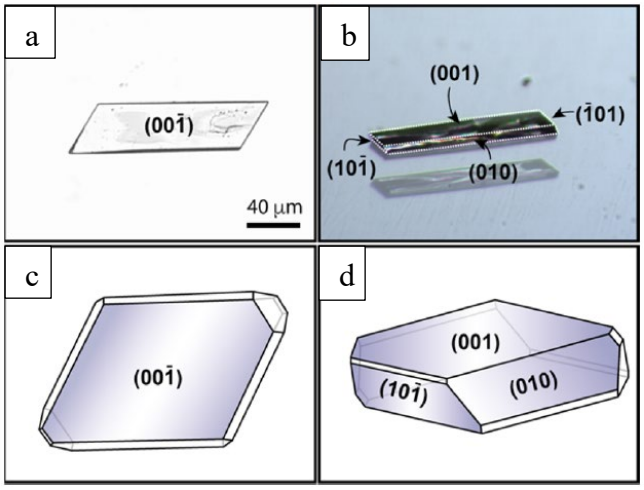

Figure 17 Furosemide morphology[36] (polymorph 1). (a) Image normal to (00^{-}1) face. (b) Magnified image with reflection. (c) Habit predicted by growth morphology method viewed normal to (00^{-}1) face. (d) Oriented habit to reveal hidden faces.

Figure 18 shows a top view of the morphology as predicted in VisualHabit using Dreiding II

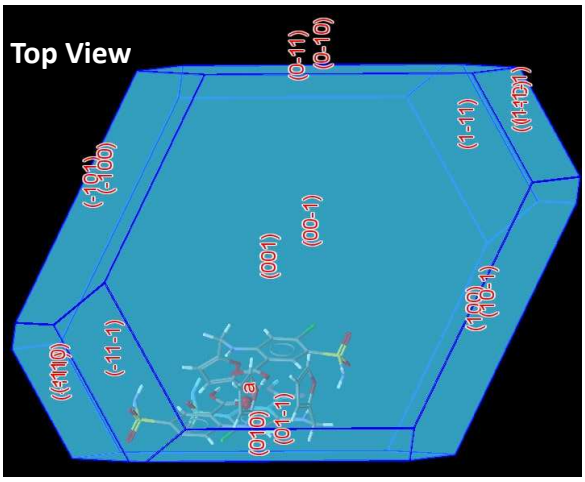

Figure 18 Furosemide morphology predicted by VisualHabit[56] within Mercury using Dreiding II potential

potential scheme. The morphology predicted by VisualHabit is very similar to the predicted morphology given in Figure 17 (c) and (d). It can be seen from the published experimental morphology that the face (001) is the most prominent face and the crystal grows longer in the direction $(10\bar{1})$. The face $(10\bar{1})$ is smaller as compared to faces (010) and (001).

The binding energies were plotted as a function of the distance from the central reference molecule to different faces of the Furosemide crystal as in Figure 19.

Figure 19 shows that most of the energy in the direction of the face (001) is occupied by the central reference slice and the molecules in slices in the positive growth direction add only a small amount of binding energy. The face $(10\bar{1})$ shows the greatest amount of binding energy. Figure 19 shows that since the binding energy for the face $(10\bar{1})$ is greatest, it is predicted to have the fastest dissolution rate whereas the face (001) has the smallest binding energy, which indicates that it has the slowest dissolution rate.

Table 4 shows the experimental dissolution rates of different faces of furosemide as reported in the literature[36]. The face $(10\bar{1})$ dissolves at the fastest rate and the face (001) dissolves at the

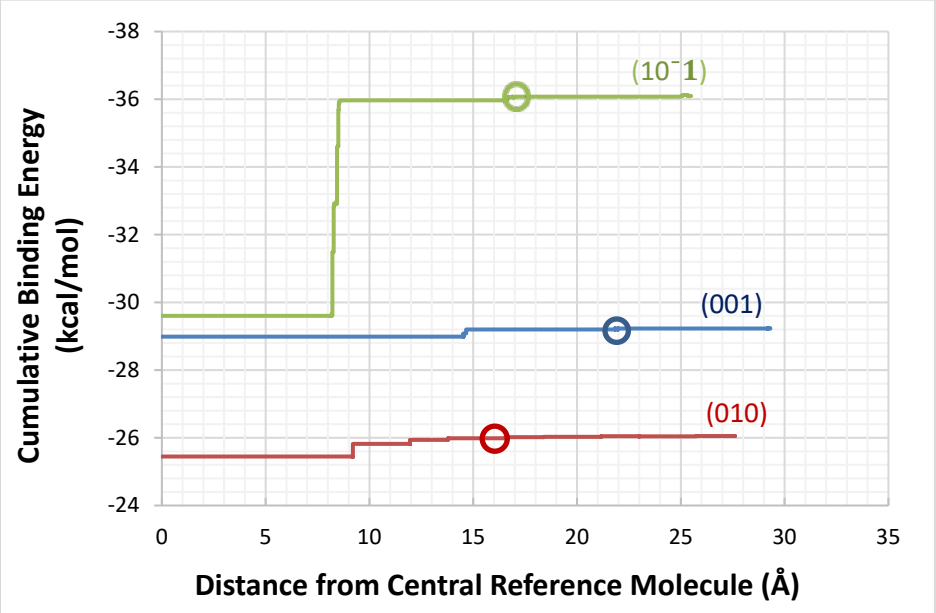

Figure 19 Binding energy loss as a function of distance from center of furosemide crystal to the faces (010), ($10^{-}1$) and (001).

slowest rate. The experimentally determined, face-specific dissolution rates have an average standard deviation of roughly 50 % due to the smaller size of the crystals chosen for the experimental dissolution rate measurements.

Table 4 Experimental Dissolution Rates of Furosemide[36]

Face	Experimental Dissolution Rates (µmol/m²s)
(10−1)	16.1 ± 6.7
(010)	12.6 ± 6.9
(001)	2.8 ± 1.4

Table 5 shows the binding energy per unit length calculations. The binding energy per unit length for the face ($10\bar{1}$) is -0.379 kcal/mol.Å, which is much greater than the values -0.034 kcal/mol.Å for the face (010) and -0.011 kcal/mol.Å for the face (001).

Table 5 Binding Energy per Unit Length Calculations

Face (hkl)	Cumulative Binding Energy (kcal/mol)	Distance from Ref. Molecule to Surface (Å)	Binding Energy per Unit Length (kcal/mol.Å)
(10-1)	-6.475	17.07	-0.379
(010)	-0.573	16.54	-0.034
(001)	-0.248	21.96	-0.011

The first row in table 6 shows the relative dissolution rate of the face $(10\overline{1})$ to the face (001). The predicted relative dissolution rate ratio is 34.45 whereas the experimental ratio is 5.75. The predicted dissolution rate ratio is 5 times greater than the experimental ratio, which is a significant discrepancy. The face $(10\overline{1})$ is much smaller in area than the face (001), so it is expected to have a significantly faster dissolution rate as compared to the face (001).

Table 6 Validation of the Predicted Relative Dissolution Rates for Furosemide

Relative Dissolution Rates	Experiment	Binding Energy Model	% Deviation between Experiment and Model
Face $(10\overline{1})$/(001)	5.75	34.45	+499.13
Face (010)/(001)	4.5	3.09	-31.33

The binding energy results are giving intrinsic dissolution rates based on the structure assuming equivalent wetting of the faces without considering the effects of the corners and edges. The predicted relative dissolution rate of the face (010) to (001) is 3.09 and the experimental value for this ratio is 4.75. Since the experimental data itself is deviating by 50 %, so this predicted value of 3.09 is falling within the possible bounds 1.36 and 13.92 based on standard deviations of the experimental results.

The predicted relative dissolution rates for two different systems, based on APIs ibuprofen and furosemide, suggest that the current simple form of the binding energy model is capable of providing a basic link between structural binding energies and dissolution rates. Out of the three relative dissolution rate ratios predicted for the two compounds in this study, two were predicted with acceptable accuracy. The third ratio had a significant discrepancy as compared to experimental results, but still provided the correct order from faster to slower dissolving faces. The discrepancy might be observed for a number of reasons, including the effect of nonequivalent wetting, the effect of corners and edges, and the effect of a large driving force for dissolution. The model is suitable for dissolution systems where the driving force for the dissolution is small and layer by layer dissolution is the rate-limiting mechanism. In such situations, the solute molecule detachment selectivity is high for different surfaces of the crystal. In the case of furosemide, dissolution was carried out under sink conditions with a large driving force, therefore greater discrepancy was observed. Whereas the driving force for dissolution was smaller in the case of ibuprofen dissolution and the predicted relative dissolution rate ratios were very close to experimental dissolution rate ratios. This suggests that, similar to the attachment energy model, the predictive ability of the binding energy model is better when the driving force is small.

6 CONCLUSIONS

Face specific dissolution kinetics of the ibuprofen single crystals have been investigated by inverted microscopy and imaging of the crystals during the dissolution process along with structural binding energy characterization using the VisualHabit software. The experiments allowed 2D visualization of the crystal morphology during the process of dissolution. During this process, images were captured and analyzed by an image analysis methodology. As a result of this, the dissolution rates were plotted as a function of the degree of undersaturation. The binding energy plots enabled the prediction of relative, face-specific dissolution rates for ibuprofen crystals. The

computational and experimental relative dissolution-rates have been quantitatively compared. It has been shown by the binding energy model that the face (011) dissolves at a faster rate compared to the face (002). The results were validated by the experiment with acceptable accuracy.

The binding energy model was then applied to a case study compound, furosemide, that has low aqueous solubility and, as a result, low bioavailability. The binding energy calculations predict that face $(10\overline{1})$ dissolves faster than the faces (010) and (001) for furosemide, which has been validated using reported experimental data but the dissolution rate ratio $(10\overline{1})$/ (001) produced a significant discrepancy compared to the experimentally determined ratio. This could be for various reasons including, the effect of nonequivalent wetting, the effect of corners and edges, and the effect of the degree of undersaturation on the experimentally measured dissolution rates. The comparison of the two sets of dissolution experiments suggested that the predictions made by model were better when the dissolution driving force was smaller.

Through the study of the solid-state binding energies within the crystals, a pathway to predict the relative dissolution rates of different faces of a crystal has been identified. This study suggests a way to understand dissolution phenomena at the molecular level that can be used to identify faster dissolving faces to design a better morphology and regulate bioavailability. The binding energy model in this study has been applied to organic crystals, but it is expected to be equally applicable to inorganic crystals. The main strength of the model in its current form is its simplicity in predicting the relative dissolution rate ratios. It produces single intrinsic dissolution rate ratios for a given API irrespective of the experimental conditions including choice of solvent, degree of undersaturation, temperature, and controlling dissolution mechanism on the surface. In a future paper, the effect of non-equivalent wetting of the crystal faces will also be considered to improve

the relative face-specific dissolution-rate prediction and the model will be applied to multiple case study dissolution systems to assess its robustness.

7 ACKNOWLEDGEMENT

The authors gratefully acknowledge a studentship for one of us, MN, funded by Pfizer and the EPSRC in the CDT for Complex Particulate Products and Processes (CP3-CDT) through grant number EP/L015285/1. We acknowledge technical support from Dr. Jonathan Pickering and Dr. Xiaojun Lai at the University of Leeds in aspects of the computational and experimental work. We also gratefully acknowledge support from Dr. Thai Thu Hien Nguyen in both computational and experimental aspects of the work.

ASSOCIATED CONTENT

Supporting Information

Calculation of perpendicular projections from the central reference plane, example of tabulated solid-state intermolecular interaction energies, experimental dissolution images of all the crystals used in this study, center to face distances vs time graphs for the crystals during dissolution, tabulated equations of straight lines fitted to dissolution graphs and face-specific experimental dissolution fluxes for ibuprofen.

AUTHOR INFORMATION

Corresponding Author

*Tel: (+44) 7588512852, E-mail: pmmn@leeds.ac.uk

Notes

The authors declare no competing financial interest

8 REFERENCES

(1) Malik, A.; Urquhart, L. Global pharma market will reach $1.12 trillion in 2022 - Pharmaceutical Commerce http://pharmaceuticalcommerce.com/business-and-finance/global-pharma-market-will-reach-1-12-trillion-2022/ (accessed Aug 31, 2018).

(2) North American Drug Delivery Technologies Market by Route of Administration & End User - 2021 | MarketsandMarkets https://www.marketsandmarkets.com/Market-Reports/north-american-drug-delivery-technologies-market-1209.html (accessed Aug 31, 2018).

(3) van Riet-Nales, D. A.; de Neef, B. J.; Schobben, A. F. A. M.; Ferreira, J. A.; Egberts, T. C. G.; Rademaker, C. M. A. Acceptability of Different Oral Formulations in Infants and Preschool Children. *Arch. Dis. Child.* **2013**, *98* (9), 725 LP – 731.

(4) Shekhawat, P. B.; Pokharkar, V. B. Understanding Peroral Absorption: Regulatory Aspects and Contemporary Approaches to Tackling Solubility and Permeability Hurdles. *Acta Pharm. Sin. B* **2017**, *7* (3), 260–280. https://doi.org/10.1016/J.APSB.2016.09.005.

(5) Hsu, J. P.; Liu, B. T. Dissolution of Solid Particles in Liquids: A Reaction-Diffusion Model. *Colloids and Surfaces* **1993**, *69* (4), 229–238. https://doi.org/10.1016/0166-6622(93)80004-Y.

(6) Siepmann, J.; Siepmann, F. Mathematical Modeling of Drug Dissolution. *Int. J. Pharm.* **2013**, *453* (1), 12–24. https://doi.org/10.1016/j.ijpharm.2013.04.044.

(7) Bird, R. B.; Stewart, W. E.; Lightfoot, E. N.; Spalding, D. B. Transport Phenomena. *Journal of Applied Mechanics*. 1961, p 317. https://doi.org/10.1115/1.3641697.

(8) Abuzar, S. M.; Hyun, S. M.; Kim, J. H.; Park, H. J.; Kim, M. S.; Park, J. S.; Hwang, S. J.

Enhancing the Solubility and Bioavailability of Poorly Water-Soluble Drugs Using Supercritical Antisolvent (SAS) Process. *Int. J. Pharm.* **2018**, *538* (1–2), 1–13. https://doi.org/10.1016/J.IJPHARM.2017.12.041.

(9) Khadka, P.; Ro, J.; Kim, H.; Kim, I.; Kim, J. T.; Kim, H.; Cho, J. M.; Yun, G.; Lee, J. Pharmaceutical Particle Technologies: An Approach to Improve Drug Solubility, Dissolution and Bioavailability. *Asian Journal of Pharmaceutical Sciences*. Shenyang Pharmaceutical University December 1, 2014, pp 304–316. https://doi.org/10.1016/j.ajps.2014.05.005.

(10) Sun, D. D.; Wen, H.; Taylor, L. S. Non-Sink Dissolution Conditions for Predicting Product Quality and In-Vivo Performance of Supersaturating Drug Delivery Systems. *J. Pharm. Sci.* **2016**, *105* (9), 2477–2488. https://doi.org/10.1016/j.xphs.2016.03.024.

(11) Almeida, L. P.; Simões, S.; Brito, P.; Portugal, A.; Figueiredo, M. Modeling Dissolution of Sparingly Soluble Multisized Powders. *J. Pharm. Sci.* **1997**, *86* (6), 726–732. https://doi.org/10.1021/js960417w.

(12) Velaga, S. P.; Djuris, J.; Cvijic, S.; Rozou, S.; Russo, P.; Colombo, G.; Rossi, A. Dry Powder Inhalers: An Overview of the In-Vitro Dissolution Methodologies and Their Correlation with the Biopharmaceutical Aspects of the Drug Products. *Eur. J. Pharm. Sci.* **2018**, *113*, 18–28. https://doi.org/10.1016/J.EJPS.2017.09.002.

(13) Hammond, R. B. Modelling Route Map: From Molecule Through the Solution State to Crystals. In *Engineering Crystallography: From Molecule to Crystal to Functional Form*; Roberts, K. J., Docherty, R., Tamura, R., Eds.; Springer Netherlands: Dordrecht, 2017; pp 71–108. https://doi.org/10.1007/978-94-024-1117-1_6.

(14) Bukovec, P.; Meden, A.; Smrkolj, M.; Vrecer, F. Influence of Crystal Habit on the

Dissolution of Simvastatin Single Crystals. *Acta Chim. Slov.* **2015**, *62* (4), 958–966.

(15) Nguyen, T. T. H.; Rosbottom, I.; Marziano, I.; Hammond, R. B.; Roberts, K. J. Crystal Morphology and Interfacial Stability of RS-Ibuprofen in Relation to Its Molecular and Synthonic Structure. *Cryst. Growth Des.* **2017**, *17* (6), 3088–3099. https://doi.org/10.1021/acs.cgd.6b01878.

(16) Maghsoodi, M. Role of Solvents in Improvement of Dissolution Rate of Drugs: Crystal Habit and Crystal Agglomeration. *Adv. Pharm. Bull.* **2015**, *5* (1), 13–18. https://doi.org/10.5681/apb.2015.002.

(17) O'Mahony, M.; Seaton, C. C.; Croker, D. M.; Veesler, S.; Rasmuson, Å. C.; Hodnett, B. K. Investigating the Dissolution of the Metastable Triclinic Polymorph of Carbamazepine Using In-Situ Microscopy. *CrystEngComm* **2014**, *16* (20), 4133–4141. https://doi.org/10.1039/C4CE00062E.

(18) Elts, E.; Greiner, M.; Briesen, H. In Silico Prediction of Growth and Dissolution Rates for Organic Molecular Crystals: A Multiscale Approach. *Crystals* **2017**, *7* (10), 288. https://doi.org/10.3390/cryst7100288.

(19) Palczynski, K.; Heimel, G.; Heyda, J.; Dzubiella, J. Growth and Characterization of Molecular Crystals of Para-Sexiphenyl by All-Atom Computer Simulations. *Cryst. Growth Des.* **2014**, *14* (8), 3791–3799. https://doi.org/10.1021/cg500234r.

(20) Li, J.; Tilbury, C. J.; Kim, S. H.; Doherty, M. F. A Design Aid for Crystal Growth Engineering. *Prog. Mater. Sci.* **2016**, *82*, 1–38. https://doi.org/10.1016/J.PMATSCI.2016.03.003.

(21) Lovette, M. A.; Browning, A. R.; Griffin, D. W.; Sizemore, J. P.; Snyder, R. C.; Doherty, M. F. Crystal Shape Engineering. *Ind. Eng. Chem. Res.* **2008**, *47* (24), 9812–9833.

https://doi.org/10.1021/ie800900f.

(22) Dandekar, P.; Kuvadia, Z. B.; Doherty, M. F. Engineering Crystal Morphology. *Annu. Rev. Mater. Res.* **2013**, *43* (1), 359–386. https://doi.org/10.1146/annurev-matsci-071312-121623.

(23) Kim, S. H.; Dandekar, P.; Lovette, M. A.; Doherty, M. F. Kink Rate Model for the General Case of Organic Molecular Crystals. *Cryst. Growth Des.* **2014**, *14* (5), 2460–2467. https://doi.org/10.1021/cg500167a.

(24) Tilbury, C. J.; Green, D. A.; Marshall, W. J.; Doherty, M. F. Predicting the Effect of Solvent on the Crystal Habit of Small Organic Molecules. *Cryst. Growth Des.* **2016**, *16* (5), 2590–2604. https://doi.org/10.1021/acs.cgd.5b01660.

(25) Hammond, R. B.; Pencheva, K.; Roberts, K. J. A Structural−Kinetic Approach to Model Face-Specific Solution/Crystal Surface Energy Associated with the Crystallization of Acetyl Salicylic Acid from Supersaturated Aqueous/Ethanol Solution. *Cryst. Growth Des.* **2006**, *6* (6), 1324–1334. https://doi.org/10.1021/cg0505618.

(26) Wu, K.; Ma, C. Y.; Liu, J. J.; Zhang, Y.; Wang, X. Z. Measurement of Crystal Face Specific Growth Kinetics. *Cryst. Growth Des.* **2016**, *16* (9), 4855–4868. https://doi.org/10.1021/acs.cgd.6b00189.

(27) Borchert, C.; Temmel, E.; Eisenschmidt, H.; Lorenz, H.; Seidel, M. A.; Sundmacher, K. Image-Based in Situ Identification of Face Specific Crystal Growth Rates from Crystal Populations. *Cryst. Growth Des.* **2014**, *14* (3), 952–971. https://doi.org/10.1021/cg401098x.

(28) Grohe, B.; O'Young, J.; Ionescu, D. A.; Lajoie, G.; Rogers, K. A.; Karttunen, M.; Goldberg, H. A.; Hunter, G. K. Control of Calcium Oxalate Crystal Growth by Face-Specific Adsorption of an Osteopontin Phosphopeptide. *J. Am. Chem. Soc.* **2007**, *129* (48), 14946–

14951. https://doi.org/10.1021/ja0745613.

(29) Khokhryakov, A. F.; Sokol, A. G.; Borzdov, Y. M.; Palyanov, Y. N. Morphology of Diamond Crystals Grown in Magnesium-Based Systems at High Temperatures and High Pressures. *J. Cryst. Growth* **2015**, *426*, 276–282. https://doi.org/10.1016/J.JCRYSGRO.2015.06.022.

(30) Donnay, J. D. H.; Harker, D. A New Law of Crystal Morphology Extending the Law of Bravais. *Am. Miner.* **1937**, *22* (5), 446–467.

(31) Hartman, P.; Perdok, W. G. On the Relations Between Structure and Morphology of Crystals. I. *Acta Crystallogr.* **1955**, *8* (1), 49–52. https://doi.org/10.1107/S0365110X55000121.

(32) Prasad, K. V. R.; Ristic, R. I.; Sheen, D. B.; Sherwood, J. N. Dissolution Kinetics of Paracetamol Single Crystals. *Int. J. Pharm.* **2002**, *238* (1–2), 29–41. https://doi.org/10.1016/S0378-5173(02)00053-4.

(33) Raghavan, S. L.; Ristic, R. I.; Sheen, D. B.; Sherwood, J. N. Dissolution Kinetics of Single Crystals of α-Lactose Monohydrate. *J. Pharm. Sci.* **2002**, *91* (10), 2166–2174. https://doi.org/10.1002/jps.10208.

(34) Østergaard, J.; Ye, F.; Rantanen, J.; Yaghmur, A.; Larsen, S. W.; Larsen, C.; Jensen, H. Monitoring Lidocaine Single-Crystal Dissolution by Ultraviolet Imaging. *J. Pharm. Sci.* **2011**, *100* (8), 3405–3410. https://doi.org/10.1002/jps.22532.

(35) Greiner, M.; Choscz, C.; Eder, C.; Elts, E.; Briesen, H. Multiscale Modeling of Aspirin Dissolution: From Molecular Resolution to Experimental Scales of Time and Size. *CrystEngComm* **2016**, *18* (28), 5302–5312. https://doi.org/10.1039/C6CE00710D.

(36) Adobes-Vidal, M.; Maddar, F. M.; Momotenko, D.; Hughes, L. P.; Wren, S. A. C.; Poloni,

L. N.; Ward, M. D.; Unwin, P. R. Face-Discriminating Dissolution Kinetics of Furosemide Single Crystals: In Situ Three-Dimensional Multi-Microscopy and Modeling. *Cryst. Growth Des.* **2016**, *16* (8), 4421–4429. https://doi.org/10.1021/acs.cgd.6b00543.

(37) Maddar, F. M.; Adobes-Vidal, M.; Hughes, L. P.; Wren, S. A. C.; Unwin, P. R. Dissolution of Bicalutamide Single Crystals in Aqueous Solution: Significance of Evolving Topography in Accelerating Face-Specific Kinetics. *Cryst. Growth Des.* **2017**, *17* (10), 5108–5116. https://doi.org/10.1021/acs.cgd.7b00401.

(38) Snyder, R. C.; Veesler, S.; Doherty, M. F. The Evolution of Crystal Shape During Dissolution: Predictions and Experiments. *Cryst. Growth Des.* **2008**, *8* (4), 1100–1101. https://doi.org/10.1021/cg7008495.

(39) Noyes, A. A.; Whitney, W. R. The Rate of Solution of Solid Substances in Their Own Solutions. *J. Am. Chem. Soc.* **1897**, *19* (12), 930–934. https://doi.org/10.1021/ja02086a003.

(40) Greiner, M.; Elts, E.; Briesen, H. Insights into Pharmaceutical Nanocrystal Dissolution: A Molecular Dynamics Simulation Study on Aspirin. *Mol. Pharm.* **2014**, *11* (9), 3009–3016. https://doi.org/10.1021/mp500148q.

(41) Holmberg, N.; Chen, J.-C.; Foster, A. S.; Laasonen, K. Dissolution of NaCl Nanocrystals: An Ab Initio Molecular Dynamics Study. *Phys. Chem. Chem. Phys.* **2014**, *16* (33), 17437–17446. https://doi.org/10.1039/C4CP00635F.

(42) Gao, Y.; Olsen, K. W. Molecular Dynamics of Drug Crystal Dissolution: Simulation of Acetaminophen Form I in Water. *Mol. Pharm.* **2013**, *10* (3), 905–917. https://doi.org/10.1021/mp4000212.

(43) Rosbottom, I.; Pickering, J. H.; Etbon, B.; Hammond, R. B.; Roberts, K. J. Examination of Inequivalent Wetting on the Crystal Habit Surfaces of RS-Ibuprofen Using Grid-Based

Molecular Modelling. *Phys. Chem. Chem. Phys.* **2018**, *20* (17), 11622–11633. https://doi.org/10.1039/C7CP08354H.

(44) Hartman, P.; Perdok, W. G. On the Relations Between Structure and Morphology of Crystals. II. *Acta Crystallogr.* **1955**, *8* (9), 521–524. https://doi.org/10.1107/S0365110X55001679.

(45) Berkovitch-Yellin, Z. Toward an Ab Initio Derivation of Crystal Morphology. *J. Am. Chem. Soc.* **1985**, *107* (26), 8239–8253. https://doi.org/10.1021/ja00312a070.

(46) Hartman, P.; Bennema, P. The Attachment Energy as a Habit Controlling Factor: I. Theoretical Considerations. *J. Cryst. Growth* **1980**, *49* (1), 145–156. https://doi.org/10.1016/0022-0248(80)90075-5.

(47) Wulff, G. Zur Frage Der Geschwindigkeit Des Wachsthums Und Der Auflösung Der Krystallflächen. *Zeitschrift für Krist. Mater.* **1901**, *34* (1–6), 449–530.

(48) Camacho Corzo, D. M.; Ma, C. Y.; Ramachandran, V.; Mahmud, T.; Roberts, K. J. Crystallisation Route Map. In *Engineering Crystallography: From Molecule to Crystal to Functional Form*; Roberts, K. J., Docherty, R., Tamura, R., Eds.; NATO Science for Peace and Security Series A: Chemistry and Biology. Springer: Dordrecht, 2017; Vol. PartF1, pp 179–213. https://doi.org/10.1007/978-94-024-1117-1_11.

(49) Clydesdale, G.; Roberts, K. J.; Docherty, R. Modelling the Morphology of Molecular Crystals in the Presence of Disruptive Tailor-Made Additives. *J. Cryst. Growth* **1994**, *135* (1–2), 331–340. https://doi.org/10.1016/0022-0248(94)90760-9.

(50) Clydesdale, G.; Roberts, K. J. Modelling the Habit Modification of Molecular Crystals by the Action of "Tailor-Made" Additives. In *Science and Technology of Crystal Growth*; Springer Netherlands, 1995; pp 179–192. https://doi.org/10.1007/978-94-011-0137-0_14.

(51) Docherty, R.; Cldesdale, G.; Roberts, K. J.; Bennema, P. Application of BFDH, Attachment Energy and Ising Models to Predicting and Understanding the Morphology of Molecular Crystals. *J. Phys. D Appl. Phys.* **1991**, *24*, 89–99.

(52) Nguyen, T. T. H. Influence of Crystallisation Environment on the Nucleation and Growth of Single Crystals of (RS)-Ibuprofen. Ph.D. Dissertation, University of Leeds, 2013.

(53) Turner, T. D.; Nguyen, T. T. H.; Nicholson, P.; Brown, G.; Hammond, R. B.; Roberts, K. J.; Marziano, I. A Temperature-Controlled Single-Crystal Growth Cell for the In-Situ Measurement and Analysis of Face-Specific Growth Rates. *J. Appl. Cryst* **2019**, *52*, 463–467. https://doi.org/10.1107/S1600576719002048.

(54) Nguyen, T. T. H.; Hammond, R. B.; Roberts, K. J.; Marziano, I.; Nichols, G. Precision Measurement of the Growth Rate and Mechanism of Ibuprofen {001} and {011} as a Function of Crystallization Environment. *CrystEngComm* **2014**, *16* (21), 4568–4586. https://doi.org/10.1039/C4CE00097H.

(55) Macrae, C. F.; Sovago, I.; Cottrell, S. J.; Galek, P. T. A.; McCabe, P.; Pidcock, E.; Platings, M.; Shields, G. P.; Stevens, J. S.; Towler, M.; et al. Mercury 4.0: From Visualization to Analysis, Design and Prediction. *J. Appl. Crystallogr.* **2020**, *53* (1), 226–235.

(56) Clydesdale, G.; Roberts, K. J.; Docherty, R. HABIT95 — A Program for Predicting the Morphology of Molecular Crystals as a Function of the Growth Environment. *J. Cryst. Growth* **1996**, *166* (1–4), 78–83. https://doi.org/10.1016/0022-0248(96)00056-5.

(57) Pickering, J.; Hammond, R. B.; Ramachandran, V.; Soufian, M.; Roberts, K. J. Synthonic Engineering Modelling Tools for Product and Process Design. In *NATO Science for Peace and Security Series A: Chemistry and Biology*; Springer Verlag, 2017; Vol. PartF1, pp 155–176.

(58) Dudognon, E.; Danède, F.; Descamps, M.; Correia, N. T. Evidence for a New Crystalline Phase of Racemic Ibuprofen. *Pharm. Res.* **2008**, *25* (12), 2853–2858. https://doi.org/10.1007/s11095-008-9655-7.

(59) Lee, T.; Ying, H. C.; Chyong, W. Z. Solubility, Polymorphism, Crystallinity, Crystal Habit, and Drying Scheme of (R, S)-(±)-Sodium Ibuprofen Dihydrate. *Pharm. Technol.* **2007**, *31* (6), 72–87. https://doi.org/10.1201/b13475-7.

(60) Oparin, R. D.; Ivlev, D. V.; Vorobei, A. M.; Idrissi, A.; Kiselev, M. G. Screening of Conformational Polymorphism of Ibuprofen in Supercritical CO2. *J. Mol. Liq.* **2017**, *239*, 49–60. https://doi.org/10.1016/j.molliq.2016.10.132.

(61) Garekani, H. A.; Sadeghi, F.; Badiee, A.; Mostafa, S. A.; Rajabi-Siahboomi, A. R.; Rajabi-Siahboomi, A. R. Crystal Habit Modifications of Ibuprofen and Their Physicomechanical Characteristics. *Drug Dev. Ind. Pharm.* **2001**, *27* (8), 803–809. https://doi.org/10.1081/DDC-100107243.

(62) McConnell, J. F. 2-(4-Isobutylphenyl) Propionic Acid. *Cryst. Struct. Commun.* **1974**, *3*, 73–75.

(63) Wilkins, S. J.; Coles, B. A.; Compton, R. G.; Cowley, A. Mechanism and Kinetics of Salicylic Acid Dissolution in Aqueous Solution under Defined Hydrodynamic Conditions via Atomic Force Microscopy: The Effects of the Ionic Additives NaCl, LiCl and MgCl2, the Organic Additives 1-Propanol, 2-Propanol, and the Surfactant Sodium Dodecyl Sulfate. *J. Phys. Chem. B* **2002**, *106* (18), 4763–4774. https://doi.org/10.1021/jp0139585.

(64) B.K.Sarojini, H.S. Yathirajan, B.Narayanna, K.Sunil, M. B. CCDC 657920: Experimental Crystal Structure Determination. *CSD Commun.* **2007**. https://doi.org/10.5517/ccq2m7m.

For Table of Contents Use Only

Title: "Impact of Structural Binding Energies on Dissolution Rates for Single Faceted-Crystals"

Author(s): Najib, Muhammad; Hammond, Robert; Mahmud, Tariq; Izumi, Toshiko

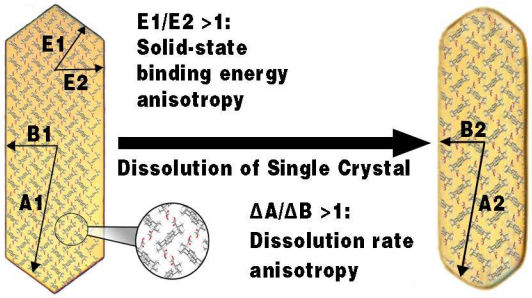

TOC Image

Synopsis

A model to calculate the intermolecular solid-state binding energies is presented to predict the relative face-specific dissolution rates of single faceted-crystals. The model was validated against face-specific dissolution rate data for ibuprofen in 95% ethanol: water (v/v) solution collected in this study and furosemide in water obtained from the literature. The model was successful on most occasions in correctly predicting the dissolution rate ratios.